














Cite this: *EES Catal.*, 2023,
1, 765

A survey of Earth-abundant metal oxides as oxygen evolution electrocatalysts in acidic media (pH < 1)[†]

Jiahao Yu, ^{ab} Stefano Giancola, ^a Bahareh Khezri, ^{ab} David Nieto-Castro, ^a Jesús Redondo, ^{cd} Frederik Schiller, ^{ei} Sara Barja, ^{cef} Maria Chiara Spadaro, ^g Jordi Arbiol, ^{gh} Felipe A. Garcés-Pineda ^{*a} and José Ramón Galán-Mascarós ^{*ah}

Electrolytic hydrogen appears as one of the most promising options to store renewable energy. In this water splitting process, the sluggish kinetics of the 4-electron oxygen evolution reaction (OER) with its high overpotentials have been widely regarded as the bottleneck to facilitate a fast, energy-efficient process. In alkaline media, numerous earth-abundant metal oxides are efficient OER catalysts, stabilized by the high concentration of hydroxide anions in the electrolyte. However, under acidic conditions, where the hydrogen evolution reaction (HER) is technologically preferred, only noble metal-based oxides (RuO₂ and IrO₂) are suitable OER catalysts, putting into question the scalability to wide-spread applications due to their scarcity and high cost. Most earth abundant metal oxides dissolve at high proton concentrations. A promising strategy to avoid this drawback consists of incorporating these catalysts into partially hydrophobic composite electrodes. Following this strategy, we have been able to conduct an extensive survey of the activity and stability of mono-, bi- and trimetallic earth-abundant transition metal oxides during the electrocatalytic OER under strongly acidic conditions. Our results confirm the general validity of the strategy by using a hydrophobic electrode to confer high stability to common metal oxides under these harsh conditions. Among all OER catalysts investigated, we found that simple manganese oxides appeared as the most active also exhibiting high, long-term stability. In particular, the stability of Mn₂O₃ oxide in the OER in acidic media was well confirmed by post-electrolysis characterization data.

Received 9th May 2023,
Accepted 12th July 2023

DOI: 10.1039/d3ey00101f

rsc.li/eescatalysis

Broader context

Acidic water electrolysis from electrolytes with high proton concentration has advantages in hydrogen production. However, only noble metals (typically iridium) are viable oxygen evolution (OER) catalysts to promote acidic water oxidation, limiting the techno-economic development of this technology. We are introducing a novel strategy to stabilize OER catalysts from earth abundant transition metals, by blending them into a partially hydrophobic electrode support. Under these conditions, we have investigated a variety of mono-, bi- and trimetallic oxides, to discover that Mn₂O₃ is the most active phase, reaching a competitive performance when compared with IrO_x, with a remarkable performance stability for over 24 h. The implementation of an analogous approach towards real electrolyzers may open promising opportunities for the substitution of noble metals by economic, viable counterparts.

^a Institute of Chemical Research of Catalonia (ICIQ-CERCA), The Barcelona Institute of Science and Technology (BIST), Av. Països Catalans 16, 43007 Tarragona, Spain.
E-mail: fgarcés@icq.es, jrgalan@icq.es

^b Departament de Química Física i Inorgànica, Universitat Rovira i Virgili, Marcel·lí Domingo 1, 43007 Tarragona, Spain

^c Department of Polymers and Advanced Materials, Centro de Física de Materiales, University of the Basque Country UPV/EHU, 20018 San Sebastián, Spain

^d Department of Surface and Plasma Science, Faculty of Mathematics and Physics, Charles University, 18000, Prague 8, Czech Republic

^e Donostia International Physics Center (DIPC), 20018 San Sebastian, Spain

^f IKERBASQUE, Basque Foundation for Science, 48009 Bilbao, Spain

^g Catalan Institute of Nanoscience and Nanotechnology (ICN2), CSIC and BIST, Campus UAB, Bellaterra, 08193 Barcelona, Catalonia, Spain

^h ICREA, Passeig Lluís Companys, 23, 08010 Barcelona, Spain

ⁱ Centro de Física de Materiales (CSIC-UPV-EHU) and Materials Physics Center (MPC), 20018 San Sebastián, Spain

[†] Electronic supplementary information (ESI) available. See DOI: <https://doi.org/10.1039/d3ey00101f>



Introduction

Electrolytic hydrogen from water splitting is in high demand to support the deployment of renewable energy as an energy storage medium, in the required transition from fossil fuels.^{1,2} One of the challenges in water electrolysis remains the oxidation catalysts for the anodic oxygen evolution reaction (OER). This 4-electron process is one of the main causes for the slow kinetics and high overpotentials.³ Competitive catalysts from earth abundant materials are required for a viable, large-scale deployment of water electrolyzers.

Numerous earth-abundant materials are able to work as OER electrocatalysts in alkaline media, reaching excellent performance, for instance the family of nickel-iron mixed oxides or (oxo) hydroxides.^{4–7} But alkaline technologies have several disadvantages, such as the need for corrosive media (hot, concentrated KOH solutions), and the relatively low current densities achieved, as limited by the OH[−] transport through the separator/anion-exchange membrane. Significantly higher current densities can be achieved under acidic conditions, thanks to the ultrafast proton transport through a proton exchange solid electrolyte (membrane) and the high proton concentration available for hydrogen generation (HER).⁸ However, only IrO₂-based catalysts are efficient and stable under these conditions. At low pH, inexpensive metal oxides suffer serious dissolution and deactivation, particularly when working at high potentials/current densities.^{9–11}

Several strategies have been proposed to stabilize earth-abundant metal oxides as OER electrocatalysts in acidic media.^{12–18} Crystalline nickel manganese antimonate on antimony-doped tin oxide (ATO) became stable at current densities of 10 mA cm^{−2} for 168 h in 1 M H₂SO₄, finely tuning the metal ratio.¹² Co₂MnO₄ demonstrated robust performance (1500 h) at 200 mA cm^{−2} at pH 1 when supported on a Pt/Ti mesh.¹⁴ Although high overpotentials were needed, these reports are promising results towards earth-abundant OER catalysis under acidic conditions.

Recently,¹⁹ we demonstrated that the use of a hydrophobic binder in the anode composition is able to stabilize Co₃O₄, otherwise unstable under these conditions.²⁰ A Co₃O₄/CPO (graphitic carbon + paraffin oil) composite sustained a current density of up to 100 mA cm^{−2} in a 1 M H₂SO₄ electrolyte. This very same electrode architecture cannot be scaled up to industrial applications, given the intrinsic long-term instability of carbon conducting supports under the OER. But our results confirm the validity of this approach to stabilize the active catalysts at low current densities. Taking advantage of this, here we report a wide screening of first row transition metal (Mn, Fe, Co, Ni and Zn) oxides with mono-, bi- and trimetallic equimolecular composition as OER catalysts in 1 M H₂SO₄. Interestingly, we found that even Mn-based oxides appear stabilized, while otherwise were characterized as highly unstable.^{21,22} Protected by the paraffin oil, Mn₂O₃ anodes showed the best performance in terms of lower overpotentials to reach 10 mA cm^{−2}, with excellent stability (> 24 h) when working in 1 M sulfuric acid solution without a sign of fatigue or deactivation. The incorporation of a second or third metal did not improve the activity of the Mn-based oxide.

Conversely, the Mn doping was critical to improve the OER activity of some other oxides, such as FeO_x, NiO_x and FeNiO_x, with > 120 mV overpotential decrease at 10 mA cm^{−2} current density. Our results confirm the general stabilizing effect of a partially hydrophobic, conducting binder to allow earth-abundant transition metal oxides to sustain water oxidation in acidic environments.

Experimental

Synthesis

All reagents were commercially available and used as received. Mixed metal oxides were prepared by modified method available in the literature.²³ The overall metal concentration of metal (Mn, Fe, Co, Ni and Zn) nitrates was fixed as 0.0125 M, and the corresponding amount of each metallic precursor was calculated in the equivalent ratio (Table S1, ESI[†]). They were dissolved in 50 mL distilled water with constant stirring. Then, glycine (25 mM) was added into the above solutions and stirred until clear solutions were obtained. Afterwards, the solutions were heated up to 210 °C until total solvent evaporation and glycine combustion. The resulting porous dark solids were collected and calcined at 1100 °C in a tubular oven for 1 h. The synthesis of Mn₂O₃ followed an analogous procedure, but the calcination step was carried out at 600 °C. For the synthesis of Mn₃O₄ as a pure phase, we followed a different procedure: Mn(NO₃)₂·4H₂O (0.151 g) and benzimidazole (0.142 g) were dissolved into 15 mL DMF and then the homogeneous solution was transferred into a Teflon-lined stainless steel autoclave. The sealed autoclave was put into an oven and kept at 140 °C for 24 h. After cooling down to room temperature, the brown product was filtered out and washed with acetone, and then dried at 60 °C.

The composite electrodes were prepared by 2 hour ball-milling at 20 s^{−1} of a mixture of paraffin oil (20 mg), graphite powder (80 mg) and oxides (40 mg), namely, MO_x/GPO, MM'_x/GPO or MM'M''O_x/GPO (M, M', M'': Mn, Fe, Co, Ni, Zn). With Mn₂O₃ the added amount of was decreased to 10 and 20 mg, these electrodes were named as 10-Mn₂O₃/GPO and 20-Mn₂O₃/GPO, respectively.

To prepare the (Mn₂O₃ + graphite)/GC (glassy carbon) electrode, graphite powder (80 mg) and Mn₂O₃ (40 mg) were mixed by ball milling firstly. Then, 10 mg of above mixture, 25 µL Nafion 117 containing solution and 975 µL ethanol aqueous solution (3:1 in volume) were sonicated for 30 min to obtain dispersed black ink. Finally, 7 µL ink was drop-cast on the GC electrode for comparison experiments.

Electrochemistry

All electrochemical experiments were performed under ambient conditions using a Bio-Logic VMP3 multichannel potentiostat and implemented with a three-electrode configuration using 1 M H₂SO₄ (pH 0.1) as the electrolyte solution, carbon rod as the counter electrode, Ag/AgCl (3 M KCl) as the reference electrode and a pocket working electrode (0.07 cm² surface area and 4 mm depth) filled with the GPO composites. The actual



mass amounts of the MO_x/GPO , $\text{MM}'\text{O}_x/\text{GPO}$ and $\text{MM}'\text{M}''\text{O}_x/\text{GPO}$ composites in the electrode pocket were measured with an analytical weight balance and indicated in Table S1 (ESI†). Although it is difficult to estimate the actual active layer, an estimation is suggested that 1/8 of the total electrode pocket volume is used as the maximum limit in contact with the solution in order to determine the mass loading for comparison.¹⁷ All potentials were measured *versus* the Ag/AgCl electrode and converted to the RHE reference scale using $E_{\text{RHE}} = E_{\text{Ag/AgCl}} + 0.21 + 0.059 \text{ pH}$ (V) while overpotentials $\eta = E_{\text{RHE}} - 1.23 \text{ V}$. Every LSV (linear sweep voltammetry) curve was recorded with a 1 mV s^{-1} scan rate for activity comparison after 10-CV (cyclic voltammetry) cycle activation. All current densities were calculated based on the geometrical surface area of the electrodes. The Ohmic drop was determined for all electrochemical data by using the automatic current interrupt (CI) software (Table S1, ESI†). The iR drop, experimentally determined using the CI technique, was corrected for all the electrodes. Tafel slopes were estimated from the LSV curves by plotting overpotential η vs. $\log j$ (j = current density). The potential vs. RHE to drive 1 mA cm^{-2} was used to define onset potential. Chronopotentiometry tests were carried out at fixed current density of 10 mA cm^{-2} . For the electrochemical double-layer capacitance (EDLC) measurements, open circuit potentials (OCPs) vs. the Ag/AgCl were firstly recorded for 30 min to reach rather stable values. Then CV experiments were carried out with 50 mV s^{-1} scan rate. Combined with above CV measurements, the 100 mV potential windows centered at OCPs could be determined and cyclic voltammetry were then carried out under scanning rates of 20, 40, 60, 80 and 100 mV s^{-1} . The current density differences between the minimum and maximum values at OCPs vs. the Ag/AgCl and the corresponding scanning rates were plotted to calculate the EDLC value (1/2 of the slope of current density–scan rate plots).²⁴ Electrochemical impedance spectroscopy (EIS) was performed by means of a typical three-electrode cell in the frequency range from 200 kHz to 100 mHz with 6 points per decade under OCP after CV activation. CVs were collected between 50 and 200 mV s^{-1} and the surface concentration of redox active Mn centers was extracted from the slope of the linear relationship between the peak current of the reduction wave and the scan rate,²⁵ according to the following equation:

$$\text{Slope} = \frac{n^2 F^2 A \Gamma_0}{4RT} \quad (1)$$

where $n = 1$; F = Faraday's constant (96485 C mol^{-1}); A = electrode surface area (0.07 cm^2); Γ_0 = surface concentration (mol cm^{-2}); R = ideal gas constant ($0.082 \text{ atm L K}^{-1} \text{ mol}^{-1}$); and T = temperature (293 K).

The turnover frequency (TOF) per active site was calculated using the equation

$$\text{TOF} = \frac{I}{mnF} \quad (2)$$

where I is the current (A) during the linear sweep voltammetry (LSV) tests, n is the number of Mn active sites (mol), F is the Faraday constant (96485 C mol^{-1}), m is 4 for oxygen evolution.²⁶

Faradaic efficiency

In order to evaluate the faradaic efficiency towards oxygen production, the chronopotentiometric experiment was carried out applying a fixed current (10 mA cm^{-2}) while the oxygen concentration in the headspace was measured *in situ* by using an Ocean Optics NeoFOX sensing system equipped with an FOSPOR probe. The FOSPOR probe was calibrated with a two-point calibration, fixing 0% O_2 under N_2 flow and 20.9% O_2 in air. The experiment was performed in a home-made H-type cell with a frit glass separating both compartments and a connection for the sensor to be inserted in the anodic gas headspace ($\sim 2.5 \text{ mL}$) (Fig. S1, ESI†). The solution was completely deaerated by purging with N_2 before starting the experiment, for at least 1 h. Then N_2 flow was removed and a base line of 10 min was recorded before starting the chronoamperometry.

The mols of O_2 generated during the electrochemical experiment were calculated *via* the following equation, considering ideal gas behavior:

$$n_{\text{O}_2, \text{exp}} = \% \text{ O}_2 \cdot P_{\text{total}} \cdot V_{\text{gas space}} \cdot R^{-1} T^{-1} / 100 \quad (3)$$

where % O_2 is given by the FOSPOR probe, P_{total} is 1 atm, $V_{\text{gas space}}$ (litres) is measured for each experiment, R is $0.082 \text{ (atm L K}^{-1} \text{ mol}^{-1})$ and T is 293 K. The faradaic oxygen production curve was calculated taking into account the charge data from the chronoamperometry experiment as described in the following equation:

$$n_{\text{O}_2, \text{far}} = Q n_e^{-1} F^{-1} \quad (4)$$

where Q (C) is the charge passed through the system, n_e is the number of mols of electrons involved in the water oxidation reaction to generate one mol of oxygen (4) and F is the Faraday constant (96485 C mol^{-1}).

Then faradaic efficiency (in %), FE, is calculated as follows:

$$\text{FE} = \frac{100 \times n_{\text{O}_2, \text{exp}}}{n_{\text{O}_2, \text{far}}} \quad (5)$$

Physical characterization

Powder X-ray diffraction (PXRD) data were recorded with a Bruker D8 Advance Series equipped with a VANTEC-1 PSD3 detector. Elemental analyses were carried out on an Agilent (ICPMS7900) inductively coupled plasma spectrometer with a mass detector (ICP-MS) at the University of Valencia. X-ray photoelectron spectroscopy (XPS) was carried out holding the sample at room temperature and illuminating it with a monochromatized Al $K\alpha$ source ($h\nu = 1486.6 \text{ eV}$) from a microfocus setup (SPECS Focus 600). The excited photo-electrons were collected by a SPECS 150 hemispherical analyzer at emission and incidence angles of 40° and 60° , respectively. The powder electrodes were deposited on top of indium tape for the XPS measurements. High resolution transmission electron microscopy (HRTEM) and scanning transmission electron microscopy (STEM) investigations were performed on a field emission gun FEI Tecnai F20 microscope. High angle annular dark-field (HAADF) STEM was combined with electron energy loss spectroscopy (EELS) on a Tecnai microscope



by using a GATAN QUANTUM energy filter in order to obtain compositional maps.

Results and discussion

Metal oxide preparation

It has been well documented that catalyst preparation and processing may affect electrochemical performance.^{27–32} To minimize synthetic effects, all oxides for this survey were prepared by the very same combustion methodology.²² We prepared twenty five oxides in total with the following ratio among reagents: MO_x (monometallic); MM'O_x (50 : 50 ratio); and MM'M''O_x (33 : 33 : 33 ratio).

Although this method did not yield completely homogeneous materials for each composition, we chose it as a common method for all materials, to minimize performance differences originated from the use different synthetic preparation methods. The dominant crystalline phases in the products were identified by powder X-ray diffraction (PXRD) and assigned to Powder Diffraction File (PDF) cards (Fig. S2–26, ESI†). According to the structural data, most of the materials contained single crystalline phases (Table 1) with some exceptions. Metal composition was determined by energy-dispersive X-ray (EDX) spectra, and in good agreement with the reagent ratio (Fig. S7–S26 and Table S1, ESI†).

The oxides were mixed with graphite (G) and paraffin oil (PO) in the desired ratio (see the Experimental section) to obtain homogeneous composites (MO_x/GPO, MM'O_x/GPO and MM'M''O_x/GPO) to be inserted into the pocket of a working electrode.

Comparative OER performance

We applied the same experimental protocol to collect the linear sweep voltammetry (LSV) for all of the oxide electrodes in 1 M

H₂SO₄ electrolyte (Fig. 1). In the monometallic series, we observed that MnO_x shows a pre-catalytic, reversible event that we assigned to a Mn³⁺/Mn⁴⁺ oxidation (Fig. 1a). MnO_x/GPO offered the best voltage efficiency, reaching ≈ 50 mA cm^{−2} at 1.73 V although the pre-catalytic event does not allow the onset potential to be directly estimated. All other oxides showed onset potentials > 1.55 V (vs. RHE) with current densities below 20 mA cm^{−2} at 1.73 V vs. RHE (Fig. 1b and Table 2), with decreasing activity as Co > Fe > Zn > Ni. The H₂SO₄ electrolyte used does not contain metallic impurities, precluding Fe uptake, well known to enhance the activity of NiO_x phases.³³

In the bimetallic oxide series, the highest current density was found for the CoNiO_x, reaching 23 mA cm^{−2} at 1.73 V vs. RHE (Fig. 1b), still far from the activity found in MnO_x/GPO electrodes. Meanwhile, pre-catalytic oxidation peaks were found for all Mn-containing catalysts, in which MnFeO_x, MnCoO_x, MnNiO_x showed quite similar activities. The rest of the series exhibited lower performance (Table 2). The FeNi oxide, which is regarded as most efficient OER electrocatalyst in alkaline media, appeared to offer the best performance before 1.7 V and then be overpassed by CoNi and MnNi oxides.^{7,34,35}

The trimetallic series (Fig. 1c), follows the same trend with the appearance of a pre-catalytic event in Mn-containing oxides. In this case, the highest activity was found for MnNiZnO_x, reaching 27 mA cm^{−2} at 1.73 V vs. RHE. No material exhibited an electrocatalytic OER performance matching that of MnO_x/GPO electrodes.

Beyond activity, stability is a crucial feature required for OER electrocatalysts. To evaluate this, we used the benchmarking protocol proposed by Jaramillo *et al.*,^{6,36} comparing the evolution of overpotential during a 2 h chronopotentiometry at 10 mA cm^{−2}. The results for the most active electrodes are shown in Fig. S27 (ESI†), with their benchmarking comparison with other electrocatalysts in recent literature (Fig. 2). We found good stability for all oxides examined in this survey, suggesting the validity of the approach: a hydrophobic binder/surface confers great stability to (almost) all metal oxides during the OER under extremely acidic conditions, opening an interesting strategy towards future applications. Some oxides (such as MnZnO_x, CoZnO_x) improved their activity during the tests. We selected MnO_x/GPO as the best performing catalyst for further studies, to better define structure/performance correlations.

OER with Mn oxides in 1 M H₂SO₄

As described before (Table 1 and Fig. S2, ESI†), the MnO_x obtained with our standardized synthetic method was indeed a mixture of two crystalline phases, Mn₂O₃ and Mn₃O₄. We prepared the Mn₂O₃ and Mn₃O₄ single phases to identify their actual OER catalytic activity. We used two different synthetic protocols to obtain pure phases of each. GPO electrodes were prepared and characterized following the same previous protocols.

After 10-cycle CV activation (Fig. S28, ESI†), LSV data of Mn₂O₃/GPO and Mn₃O₄/GPO were measured and collected. The results indicated that Mn₂O₃/GPO offered better OER activity, reaching a current density of 124 mA cm^{−2} at 1.73 V (Fig. 3a). Interestingly, the Mn₃O₄/GPO electrodes offered instead analogous

Table 1 The feeding metal ratio in syntheses and crystalline phases found by X-ray diffraction analysis

Catalyst	Crystalline phases found
MnO _x	Mn ₂ O ₃ , Mn ₃ O ₄
FeO _x	Fe ₂ O ₃
CoO _x	Co ₃ O ₄
NiO _x	NiO
ZnO _x	ZnO
MnFeO _x	(Mn, Fe) ₂ O ₃
MnCoO _x	(Co, Mn) ₃ O ₄
MnNiO _x	Ni ₆ MnO ₈
MnZnO _x	ZnMnO ₃ , ZnMn ₃ O ₄
FeCoO _x	(Co, Fe) ₂ O ₃
FeNiO _x	NiFe ₂ O ₄
FeZnO _x	ZnFe ₂ O ₄ , ZnO
CoNiO _x	(Co, Ni)O
CoZnO _x	ZnCo ₂ O ₄ , ZnO
NiZnO _x	(Ni, Zn)O
MnFeCoO _x	(Mn, Fe, Co) ₃ O ₄
MnFeNiO _x	(Mn, Ni)Fe ₂ O ₄ , (Mn, Fe)Ni ₂ O ₄
MnFeZnO _x	ZnMn ₃ O ₄ , (Fe, Zn) _{0.85} O, MnFe ₂ O ₄
MnCoNiO _x	Ni ₆ MnO ₈ , (Co, Ni)O
MnCoZnO _x	(Mn, Zn)Co ₂ O ₄
MnNiZnO _x	Ni ₆ MnO ₈ , (Ni, Zn)O
FeCoNiO _x	(Co, Ni)Fe ₂ O ₄
FeCoZnO _x	(Fe, Co) ₂ O ₃ , ZnO
FeNiZnO _x	Fe ₃ O ₄ , (Ni, Zn)O
CoNiZnO _x	CoNiO ₂ , ZnCo ₂ O ₄ , ZnO



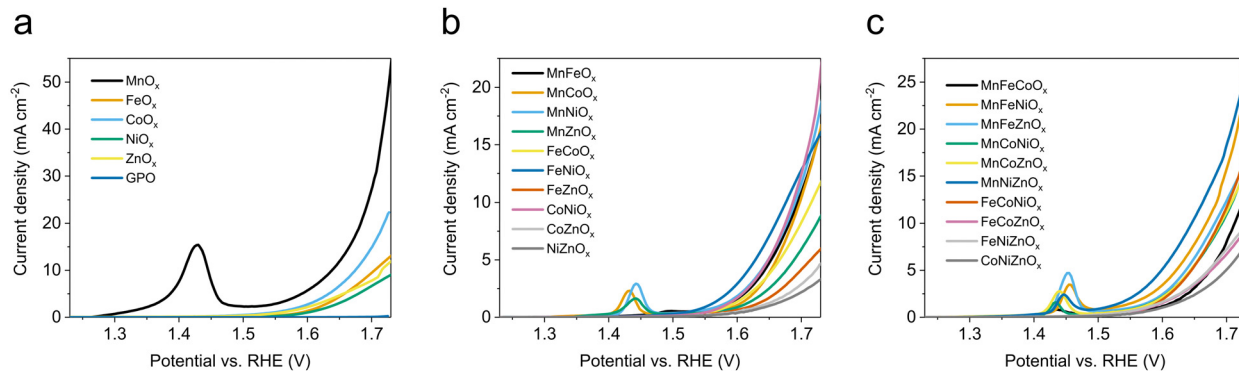


Fig. 1 LSV curves in 1 M H₂SO₄ electrolyte (pH 0.1) with 1 mV s^{−1} scan rate of (a) MO_x/GPO, (b) MM'O_x/GPO, (c) MM'M''O_x/GPO.

Table 2 Electrochemical parameters for metal-oxide/GPO electrodes. From LSV: overpotential (η_{10}) to reach $j = 10 \text{ mA cm}^{-2}$; and current density (j_{500}) at 500 mV overpotential ($\approx 1.73 \text{ V vs. RHE}$). From chronopotentiometry at $j = 10 \text{ mA cm}^{-2}$: initial overpotential ($\eta_{t=0.1}$) and overpotential after 2 h ($\eta_{t=2 \text{ h}}$)

Electrode	$\eta_{10} \text{ (V)}$ $j = 10 \text{ mA cm}^{-2}$	$j_{500} \text{ (mA cm}^{-2}\text{)}$ $\eta = 500 \text{ mV}$	$\eta_{t=0.1} \text{ (V)}$	$\eta_{t=2 \text{ h}} \text{ (V)}$
MnO _x	0.407	52	0.421	0.425
FeO _x	0.473	14	0.544	0.536
CoO _x	0.443	22	0.468	0.466
NiO _x	—	9	0.596	0.604
ZnO _x	0.486	12	0.582	0.591
MnFeO _x	0.465	16	0.485	0.466
MnCoO _x	0.467	16	0.496	0.495
MnNiO _x	0.459	18	0.488	0.480
MnZnO _x	—	9	0.546	0.488
FeCoO _x	0.485	12	0.550	0.537
FeNiO _x	0.448	16	0.537	0.548
FeZnO _x	—	6	0.615	0.588
CoNiO _x	0.454	23	0.496	0.488
CoZnO _x	—	5	0.565	0.528
NiZnO _x	—	3	0.617	0.588
MnFeCoO _x	0.484	14	0.499	0.478
MnFeNiO _x	0.437	25	0.467	0.462
MnFeZnO _x	0.453	17	0.511	0.476
MnCoNiO _x	0.462	16	0.502	0.477
MnCoZnO _x	0.462	17	0.497	0.468
MnNiZnO _x	0.417	27	0.472	0.470
FeCoNiO _x	0.458	17	0.539	0.528
FeCoZnO _x	—	9	0.537	0.518
FeNiZnO _x	—	10	0.568	0.564
CoNiZnO _x	—	8	0.558	0.533
Mn ₂ O ₃	0.328	124	0.358	0.365
Mn ₃ O ₄	0.282	74	0.438	0.432

performance to the original MnO_x/GPO electrodes. The electrochemical double-layer capacitance (EDLC) data, which are proportional to the electrochemically active area, were estimated at 29 and 10 mF cm^{−2} for Mn₂O₃/GPO and Mn₃O₄/GPO respectively (Fig. S29, ESI†). This larger EDLC may contribute to the higher electrochemical activity observed. However, this should not be the only significant effect, since other parameters point also towards a genuine better catalytic performance for Mn₂O₃/GPO.

The total density of active centers can be estimated from the Mn⁴⁺/Mn³⁺ quasi-reversible redox pair observed in the CV data (Fig. S30, ESI†). The measurements at different scan rates

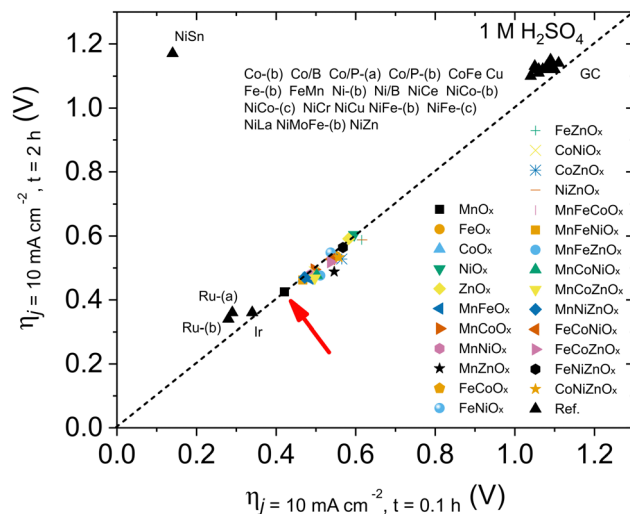


Fig. 2 Benchmarking of the activity/stability features for OER electrocatalysts in acidic media following the protocol by Jaramillo *et al.*⁶

allowed us to estimate a 172 nmol cm^{−2} density for Mn₂O₃/GPO and 100 nmol cm^{−2} density for Mn₃O₄/GPO, respectively. Besides, a higher TOF value was found for Mn₂O₃/GPO (0.0013 s^{−1}) compared to that of Mn₃O₄/GPO (0.00071 s^{−1}) under a 500 mV overpotential. In addition to the larger density of active Mn³⁺/Mn⁴⁺ centers and turnover frequency per active site, the smaller Nyquist semicircle diameter in the electrochemical impedance spectroscopy (Fig. S31, ESI†) showed a faster charge transfer for Mn₂O₃/GPO with a lower R_{ct} value of 10 Ω compared to 17 Ω of Mn₃O₄/GPO. This suggests a faster reaction mechanism also supported by the Tafel analysis: a distinct Tafel slope of 158 mV dec^{−1} was found for Mn₂O₃/GPO, much lower than the 287 mV dec^{−1} found for Mn₃O₄ (Fig. S32, ESI†). The Tafel slope is directly dependent on the kinetics of the rate-limiting step, and not on the total number of available active sites.³⁷ MnO_x/GPO electrodes showed a quite similar Tafel slope (157 mV dec^{−1}) to that of Mn₂O₃/GPO, showing the dominant contribution of the Mn₂O₃ active phase. The previous benchmarking protocol applied to Mn₂O₃/GPO showed a stable, low overpotential of $\leq 365 \text{ mV}$, to maintain

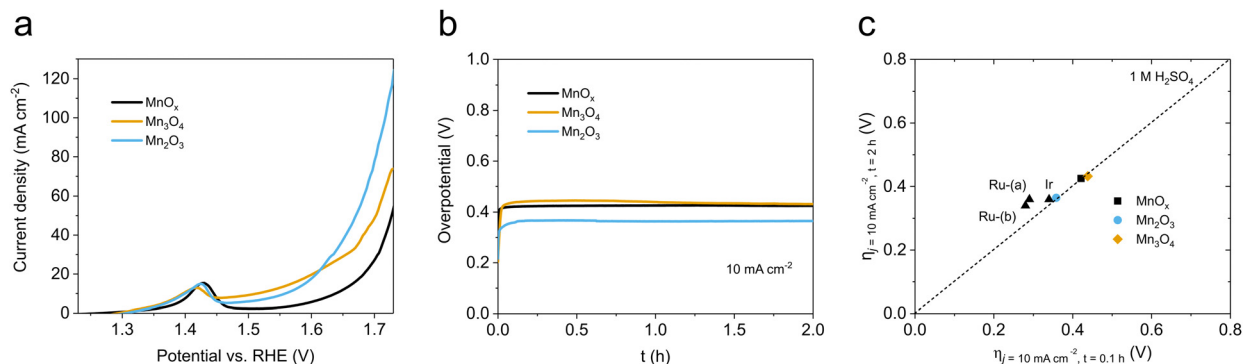


Fig. 3 (a) electrocatalytic activity of MnO_x/GPO, Mn₃O₄/GPO and Mn₂O₃/GPO; (b) stability tests of MnO_x/GPO, Mn₃O₄/GPO and Mn₂O₃/GPO in chronopotentiometry measurements at 10 mA cm⁻²; (c) benchmarking of the activity/stability features between our Mn-based oxide and noble metal-based electrocatalysts according to the study of Jaramillo *et al.*⁶

a comparable performance of noble metal (Fig. 3b and c). The long-term stability of this catalyst was also confirmed during a 24 h chronopotentiometry at 10 mA cm⁻² (Fig. S33, ESI†). Besides, this excellent stability was much better than that of other Mn-based materials towards OER in acid (Table S2, ESI†). After the benchmarking experiment, we analyzed the electrolyte content to check for any Mn leaching (Table S3, ESI†). We found the presence of Mn just at the ppb level, accounting for a maximum leaching of ≈ 0.38% of the total. With these data, we can estimate a stability number³⁸ of 130, and an activity-stability factor³⁹ of 52. An estimated lifetime of 3914 h is comparable and competitive to that of noble metal-based catalysts under analogous conditions. This is a promising performance/stability matching for noble metal oxide catalysts under acidic conditions.

To confirm the critical role of the hydrophobic binder, we performed analogous experiments with Mn₂O₃ on glassy carbon electrodes (Mn₂O₃/GC), without the addition of paraffin oil. The electrochemistry of this electrode differed significantly from that observed for the related Mn₂O₃/GPO electrode. Lower currents were reached, below 1.5 mA cm⁻² at a 500 mV overpotential (Fig. S34A, ESI†). Moreover, the Mn₂O₃/GC electrodes completely lost activity after just ~15 minutes under a 2 mA cm⁻² density (current (Fig. S34B, ESI†). This fast deactivation in the absence of the paraffin oil supports its active protective role in the GPO binder.^{19,21,22}

Finally, we measured anodic oxygen evolution during chronopotentiometry experiments with Mn₂O₃/GPO electrodes at a constant current density of 10 mA cm⁻² (Fig. S35, ESI†). >99% faradaic efficiency was obtained, confirming that the dominant catalysis process was the OER under these conditions.

Post-electrolysis Mn₂O₃/GPO characterization

We characterized the structural and chemical evolution of the Mn₂O₃/GPO electrodes after these 2 h electrolysis at 10 mA cm⁻² in 1 M H₂SO₄, further confirming the stability of Mn₂O₃ as a genuine OER catalyst. The PXRD patterns confirm the presence and stability of the Mn₂O₃ phase as no significant change nor shift were found in the observed peaks (Fig. S36, ESI†).

This suggests no evident structural changes are occurring in the bulk of the material Mn₂O₃.

We also investigated the Mn₂O₃/GPO composite after 2 h electrolysis at 10 mA cm⁻² by means of HRTEM (Fig. 4). The HRTEM images and STEM-EELS analyses also confirmed a high structural and chemical stability (Fig. S37–S41, ESI†). As we can observe in Fig. 4a, the NPs still have the orthorhombic Pbcu α-Mn₂O₃ atomic structure (S.G.: 61) imaged along its [101] zone axis. The presence of crystalline graphite has been also evidenced with the 2H oriented structure along its [0001] zone axis. In Fig. 4b both top and side views are reported and highlighted in the frequency filtered map, in red and yellow respectively. In Fig. 4c the STEM-HAADF image and STEM-EELS analysis is reported observing that the elements are homogeneously distributed confirming the atomic ratio evaluated from the HRTEM analysis. The crystalline nature of the graphite is also evidenced as it has been possible to extrapolate its contribution from the amorphous C arising from the TEM grid support. For STEM-EELS the C K edge at 284 eV (blue for amorphous and orange for graphite), O K edge at 532 eV (green) and Mn L edge at 640 eV (red) have been used. On the right side of Fig. 4c the relative composition analysis of Mn and O is also reported, to evaluate the atomic ratio of the investigated NPs. By comparing the HRTEM and STEM-EELS analysis from all the investigated samples we can observe that neither crystallinity nor particle size are affected by the electrochemical process.

We employed X-ray photoemission spectroscopy to determine the surface chemical composition of the electrodes before and after the electrocatalytic process. Fig. 5a shows the Mn 2p core-level of the Mn₂O₃/GPO composite before (ii) and after (iii) the electrochemical test. The spectra of Mn₂O₃ without the binder (i) are provided for reference.

The two main emission peaks correspond to the 2p_{3/2} and 2p_{1/2} components arising from the spin-orbit splitting. The different possible oxidation states of a transition metal in an oxide contribute to the 2p core level line shape. In this considered Mn case, this involves Mn²⁺, Mn³⁺ and Mn⁴⁺ oxidation states, which challenges the unambiguous assignment of the oxide formed (Fig. S42, ESI†). Still, the absence of satellites peaks at about 6 eV higher binding energies from 2p_{1/2} and 2p_{3/2}



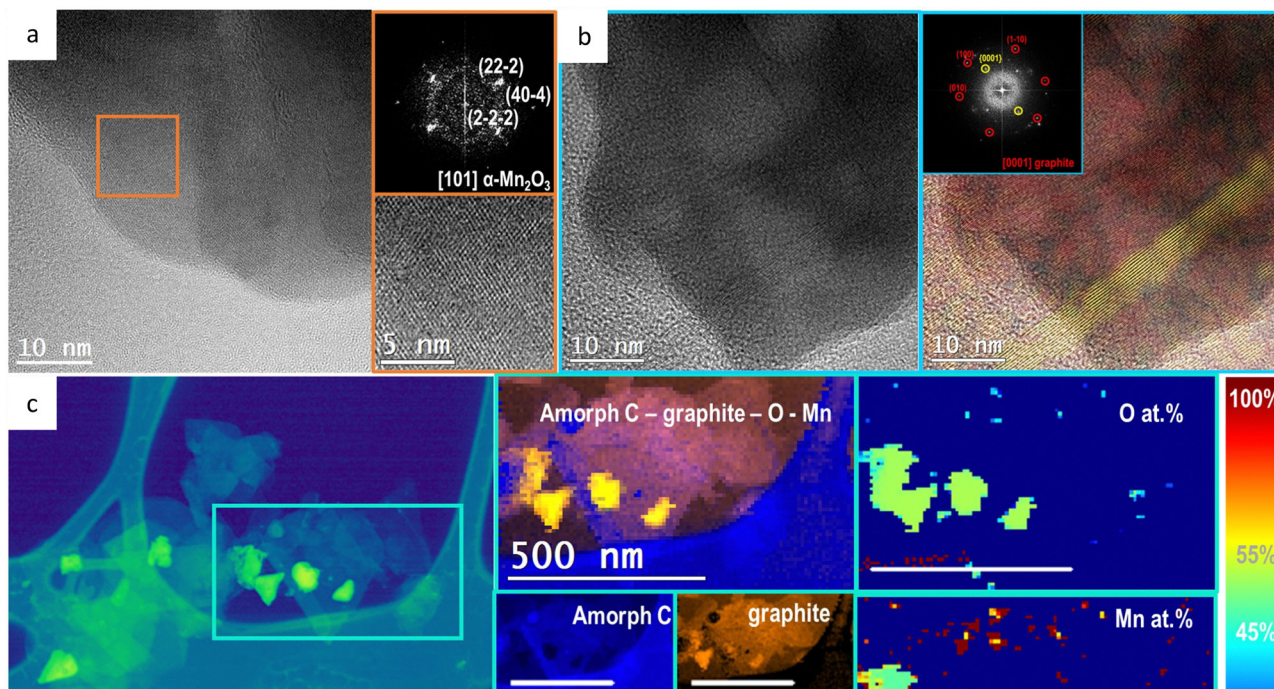


Fig. 4 (a) HRTEM general image of a Mn_2O_3 nanocrystal, with a magnified view on the bottom right and its corresponding indexed power spectrum. (b) HRTEM image showing the lattice fringes corresponding to the graphite-like structures. On the right side we present an indexed power spectrum from the same area, superposed to the obtained frequency filtered image where the found graphitic structures are shown in red and yellow, respectively. (c) False color HAADF STEM general view and the corresponding EELS composition, from relative composition analysis, for both Mn and O. (All scale bars correspond to 500 nm).

components fairly allows us to exclude the MnO phase,⁴⁰ while the observance of the Mn $2p_{1/2}$ satellite structure ($\Delta E_{2p_{1/2}\text{-sat}} \approx 10.1$ eV) supports the presence of the Mn_2O_3 phase^{41,42} identified by HRTEM analysis. Note that the apparent attenuation of the described satellite in the $\text{Mn}_2\text{O}_3/\text{GPO}$ samples is related to the

overlap with the In $3p_{3/2}$ photoemission peak from the In foil used as a sample plate (see the Experimental section).

Relevantly, we do not observe a variation of the Mn 2p line shape, nor energy shift in the binding energy of the 2p components, from the electrode after the OER compared to the as-synthesized electrode. In addition to the line shape of the Mn 2p spectra, analysis of the energy separation of the two peaks characteristics of the Mn 3s core-level has been used to identify the Mn oxidation state. Fig. 5b shows the Mn 3s spectra of the $\text{Mn}_2\text{O}_3/\text{GPO}$ composite before (ii) and after (iii) the electrochemical test, as well as the Mn_2O_3 reference (i). The energy peak separation of the Mn 3s multiplet splitting $\Delta E_{3s} \approx 5.5$ eV, constant across the three compounds, additionally supports the absence of significant changes in the oxidation state of the catalyst due to the electrochemical performance.^{41,42}

These experiments showed the bulk and functional stability of $\text{Mn}_2\text{O}_3/\text{GPO}$ electrodes during acidic OER electrocatalysis. Nevertheless, we cannot discard surface reconstruction occurring under operation conditions. This is a challenging task that will be worth investigating using appropriate techniques.⁴³

Conclusions

In summary, we have carried out a survey of earth abundant transition metal oxides as oxygen evolution electrocatalysts under acidic conditions using a conductive and partially hydrophobic support to confer on them good stability. This reliable

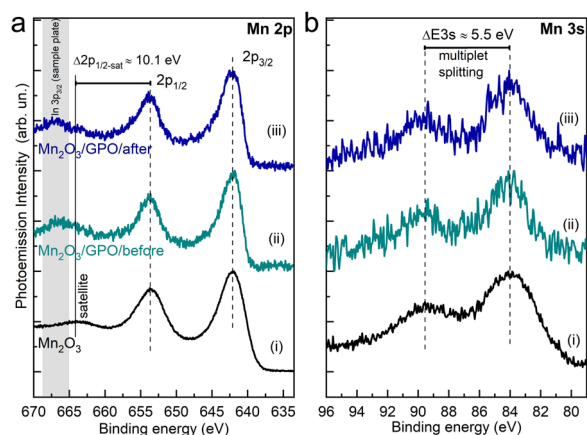


Fig. 5 XPS spectra of (a) Mn-2p and (b) Mn-3s regions of the Mn_2O_3 electrodes before (ii) and after (iii) the electrochemical performance. The spectra of the Mn oxide prior to be mixed with the graphite powder is provided as reference (i). The relative energy position of the $2p_{1/2}$ satellite and the constant magnitude of multiplet splitting in the 3s component supports the existence of a stable Mn^{3+} oxide.



strategy has allowed us to compare their electrochemical performance despite their intrinsic instability towards dissolution or deactivation. Among all the oxides tested, Mn_2O_3 -based anodes successfully passed the benchmarking protocol in acidic media and were able to deliver 10 mA cm^{-2} in 1 M sulfuric acid solution ($\text{pH} < 0.1$) at a low overpotential $\eta < 365 \text{ mV}$. Besides, the critical role of Mn doping was also found to greatly improve the acidic OER performance. These comprehensive findings will be helpful in the challenge of stabilizing earth-abundant electrocatalysts for the acidic OER, and they confirm that the promising activity of Mn centers under these conditions, superior to all the other transition metals investigated. Efficient elemental doping and structural engineering could further improve the electrocatalytic performance of Mn_2O_3 .

Author contributions

J.R.G.M. and F.A.G.P. conceived the original concept and designed the project. J.Y. and F.A.G.P. coordinated the efforts of the research team. J.Y., F.A.G.P., B.K. and D.N.C. synthesized, processed and structurally characterized the materials and electrodes. J.Y. performed the electrochemical experiments and analyzed the data. J.Y. and S.G. quantified the oxygen evolution. J.R., F.S., and S.B. collected and analyzed the XPS data. M.C.S. and J. A. collected and analyzed the TEM data. J.Y., F.A.G.P., and J.R.G.M. co-wrote the manuscript with contributions from all authors.

Conflicts of interest

There are no conflicts to declare.

Acknowledgements

The authors are thankful for the support from MCIN/AEI/10.13039/501100011033/ and “ERDF A way of making Europe” through projects RED2022-134508-T (CAT&SCALE), PID2021-124796OB-I00 and PID2020-116093RB-C43&C44 funded by MCIN/AEI/10.13039/501100011033; from the Generalitat de Catalunya (2021SGR1154 and 2021SGR00457), and from the Basque Government (IT-1591-22). S.B. acknowledges RYC-2017-21931 funded via MCIN/AEI/10.13039/501100011033 and by ESF Investing in your future and UPV/EHU project EHU-ROPE19/01. ICIQ and ICN2 are supported by the Ministerio de Ciencia e Innovación through the Severo Ochoa Excellence Accreditations CEX2019-000925-S (MCIN/AEI) and CEX2021-001214-S; and by the CERCA Programme/Generalitat de Catalunya. J.Y. thanks the China Scholarship Council (CSC) for predoctoral fellowships (File No. 201806270234). J.R. acknowledges the Czech Science Foundation and funding from PIF outgoing project number 22-180790. M.C.S. has received funding from the European Union’s Horizon 2020 research and innovation programme under Marie Skłodowska-Curie grant 754510 (PROBIST) and the Severo Ochoa programme. M.C.S. is also thankful for the funding from the postdoctoral fellowship Juan de la Cierva Incorporation from MICINN (JCI-2019)

and the Severo Ochoa programme. This study is part of the Advanced Materials programme and was supported by MCIN with funding from the European Union NextGenerationEU (PRTR-C17.I1) and the Generalitat de Catalunya.

References

- 1 Z. W. She, J. Kibsgaard, C. F. Dickens, I. Chorkendorff, J. K. Nørskov and T. F. Jaramillo, *Science*, 2017, **355**, 1–12.
- 2 S. G. Nnabuefe, J. Ugbeh-Johnson, N. E. Okeke and C. Ogbonnaya, *Carbon Capture Sci. Technol.*, 2022, **3**, 100042.
- 3 Z. Chen, L. Guo, L. Pan, T. Yan, Z. He, Y. Li, C. Shi, Z. F. Huang, X. Zhang and J. J. Zou, *Adv. Energy Mater.*, 2022, **12**, 2103670.
- 4 H. Ding, H. Liu, W. Chu, C. Wu and Y. Xie, *Chem. Rev.*, 2021, **121**, 13174–13212.
- 5 J. Yu, G. Cheng and W. Luo, *J. Mater. Chem. A*, 2017, **5**, 11229–11235.
- 6 C. C. L. McCrory, S. Jung, I. M. Ferrer, S. M. Chatman, J. C. Peters and T. F. Jaramillo, *J. Am. Chem. Soc.*, 2015, **137**, 4347–4357.
- 7 M. Gong and H. Dai, *Nano Res.*, 2015, **8**, 23–39.
- 8 C. Spöri, J. T. H. Kwan, A. Bonakdarpour, D. P. Wilkinson and P. Strasser, *Angew. Chem., Int. Ed.*, 2017, **56**, 5994–6021.
- 9 T. Reier, H. N. Nong, D. Teschner, R. Schlögl and P. Strasser, *Adv. Energy Mater.*, 2017, **7**, 1601275.
- 10 Z. Lei, T. Wang, B. Zhao, W. Cai, Y. Liu, S. Jiao, Q. Li, R. Cao and M. Liu, *Adv. Energy Mater.*, 2020, **10**, 200478.
- 11 Y. Liu, X. Liang, H. Chen, R. Gao, L. Shi, L. Yang and X. Zou, *Chinese J. Catal.*, 2021, **42**, 1054–1077.
- 12 I. A. Moreno-Hernandez, C. A. Macfarland, C. G. Read, K. M. Papadantonakis, B. S. Brunshwig and N. S. Lewis, *Energy Environ. Sci.*, 2017, **10**, 2103–2108.
- 13 M. Chatti, J. L. Gardiner, M. Fournier, B. Johannessen, T. Williams, T. R. Gengenbach, N. Pai, C. Nguyen, D. R. MacFarlane, R. K. Hocking and A. N. Simonov, *Nat. Catal.*, 2019, **2**, 457–465.
- 14 A. Li, S. Kong, C. Guo, H. Ooka, K. Adachi, D. Hashizume, Q. Jiang, H. Han, J. Xiao and R. Nakamura, *Nat. Catal.*, 2022, **5**, 109–118.
- 15 S. Pan, H. Li, D. Liu, R. Huang, X. Pan, D. Ren, J. Li, M. Shakouri, Q. Zhang, M. Wang, C. Wei, L. Mai, B. Zhang, Y. Zhao, Z. Wang, M. Graetzel and X. Zhang, *Nat. Commun.*, 2022, **13**, 2294.
- 16 J. Huang, H. Sheng, R. D. Ross, J. Han, X. Wang, B. Song and S. Jin, *Nat. Commun.*, 2021, **12**, 3036.
- 17 M. Blasco-Ahicart, J. Soriano-Lopez, J. J. Carbo, J. M. Poblet and J. R. Galan-Mascaros, *Nat. Chem.*, 2018, **10**, 24–30.
- 18 P. Y. Tang, L. J. Han, F. S. Hegner, P. Paciok, M. Biset-Peiró, H. C. Du, X. K. Wei, L. Jin, H. B. Xie, Q. Shi, T. Andreu, M. Lira-Cantú, M. Heggen, R. E. Dunin-Borkowski, N. López, J. R. Galán-Mascarós, J. R. Morante and J. Arbiol, *Adv. Energy Mater.*, 2019, **9**, 1901836.
- 19 J. Yu, F. A. Garcés-Pineda, J. González-Cobos, M. Peña-Díaz, C. Rogero, S. Giménez, M. C. Spadaro, J. Arbiol, S. Barja and J. R. Galán-Mascarós, *Nat. Commun.*, 2022, **13**, 4341.



- 20 M. Etzi Coller Pascuzzi, M. van Velzen, J. P. Hofmann and E. J. M. Hensen, *ChemCatChem*, 2021, **13**, 459–467.
- 21 L. Zhou, A. Shinde, J. H. Montoya, A. Singh, S. Gul, J. Yano, Y. Ye, E. J. Crumlin, M. H. Richter, J. K. Cooper, H. S. Stein, J. A. Haber, K. A. Persson and J. M. Gregoire, *ACS Catal.*, 2018, **8**, 10938–10948.
- 22 L. G. Bloor, P. I. Molina, M. D. Symes and L. Cronin, *J. Am. Chem. Soc.*, 2014, **136**, 3304–3311.
- 23 J. Y. C. Chen, J. T. Miller, J. B. Gerken and S. S. Stahl, *Energy Environ. Sci.*, 2014, **7**, 1382–1386.
- 24 D. M. Morales and M. Risch, *JPhys Energy*, 2021, **3**, 34013.
- 25 S. Pintado, S. Goberna-Ferrón, E. C. Escudero-Adán and J. R. Galán-Mascarós, *J. Am. Chem. Soc.*, 2013, **135**, 13270–13273.
- 26 J. Zhu, Y. Guo, F. Liu, H. Xu, L. Gong, W. Shi, D. Chen, P. Wang, Y. Yang, C. Zhang, J. Wu, J. Luo and S. Mu, *Angew. Chem., Int. Ed.*, 2021, **60**, 12328–12334.
- 27 D. Chen, R. Yu, D. Wu, H. Zhao, P. Wang, J. Zhu, P. Ji, Z. Pu, L. Chen, J. Yu and S. Mu, *Nano Energy*, 2022, **100**, 107445.
- 28 Q. Ma and S. Mu, *Interdiscip. Mater.*, 2023, **2**, 53–90.
- 29 A. Govind Rajan, J. M. P. Martinez and E. A. Carter, *ACS Catal.*, 2020, **10**, 11177–11234.
- 30 P. Wang and B. Wang, *ACS Appl. Mater. Interfaces*, 2021, **13**, 59593–59617.
- 31 Q. Xu, J. Zhang, H. Zhang, L. Zhang, L. Chen, Y. Hu, H. Jiang and C. Li, *Energy Environ. Sci.*, 2021, **14**, 5228–5259.
- 32 S. Li, Y. Gao, N. Li, L. Ge, X. Bu and P. Feng, *Energy Environ. Sci.*, 2021, **14**, 1897–1927.
- 33 L. Trotochaud, S. L. Young, J. K. Ranney and S. W. Boettcher, *J. Am. Chem. Soc.*, 2014, **136**, 6744–6753.
- 34 F. Song and X. Hu, *Nat. Commun.*, 2014, **5**, 4477.
- 35 F. A. Garcés-Pineda, H. Chuong Nguyễn, M. Blasco-Ahicart, M. García-Tecedor, M. de Fez Febré, P. Y. Tang, J. Arbiol, S. Giménez, J. R. Galán-Mascarós and N. López, *ChemSusChem*, 2021, **14**, 1595–1601.
- 36 C. C. L. McCrory, S. Jung, J. C. Peters and T. F. Jaramillo, *J. Am. Chem. Soc.*, 2013, **135**, 16977–16987.
- 37 T. Shinagawa, A. T. Garcia-Esparza and K. Takanabe, *Sci. Rep.*, 2015, **5**, 13801.
- 38 S. Geiger, O. Kasian, M. Ledendecker, E. Pizzutilo, A. M. Mingers, W. T. Fu, O. Diaz-Morales, Z. Li, T. Oellers, L. Fruchter, A. Ludwig, K. J. J. Mayrhofer, M. T. M. Koper and S. Cherevko, *Nat. Catal.*, 2018, **1**, 508–515.
- 39 Y. T. Kim, P. P. Lopes, S. A. Park, A. Y. Lee, J. Lim, H. Lee, S. Back, Y. Jung, N. Danilovic, V. Stamenkovic, J. Erlebacher, J. Snyder and N. M. Markovic, *Nat. Commun.*, 2017, **8**, 1449.
- 40 M. C. Biesinger, B. P. Payne, A. P. Grosvenor, L. W. M. Lau, A. R. Gerson and R. S. C. Smart, *Appl. Surf. Sci.*, 2011, **257**, 2717–2730.
- 41 M. A. Stranick, *Surf. Sci. Spectra*, 1999, **6**, 39.
- 42 Y. Gorlin and T. F. Jaramillo, *J. Am. Chem. Soc.*, 2010, **132**, 13612–13614.
- 43 X. Luo, X. Tan, P. Ji, L. Chen, J. Yu and S. Mu, *EnergyChem*, 2022, **5**, 100091.

